Correlation between microstructural inhomogeneity and architectural design in additively manufactured NiTi shape memory alloys

Yan, Zhaorui; Zhu, Jia Ning; Hartl, Darren; Riemslag, Ton; Scott, Sean Paul; Petrov, Roumen; Hermans, Marcel; Jovanova, Jovana; Popovich, Vera

DOI
10.1080/17452759.2024.2396065

Publication date
2024

Document Version
Final published version

Published in
Virtual and Physical Prototyping

Citation (APA)
Yan, Z., Zhu, J. N., Hartl, D., Riemslag, T., Scott, S. P., Petrov, R., Hermans, M., Jovanova, J., & Popovich, V. (2024). Correlation between microstructural inhomogeneity and architectural design in additively manufactured NiTi shape memory alloys. *Virtual and Physical Prototyping*, *19*(1), Article e2396065. https://doi.org/10.1080/17452759.2024.2396065

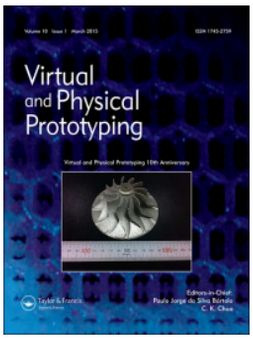

Virtual and Physical Prototyping

ISSN: (Print) (Online) Journal homepage: www.tandfonline.com/journals/nvpp20

Correlation between microstructural inhomogeneity and architectural design in additively manufactured NiTi shape memory alloys

Zhaorui Yan, Jia-Ning Zhu, Darren Hartl, Ton Riemslag, Sean Paul Scott, Roumen Petrov, Marcel Hermans, Jovana Jovanova & Vera Popovich

To cite this article: Zhaorui Yan, Jia-Ning Zhu, Darren Hartl, Ton Riemslag, Sean Paul Scott, Roumen Petrov, Marcel Hermans, Jovana Jovanova & Vera Popovich (2024) Correlation between microstructural inhomogeneity and architectural design in additively manufactured NiTi shape memory alloys, Virtual and Physical Prototyping, 19:1, e2396065, DOI: 10.1080/17452759.2024.2396065

To link to this article: https://doi.org/10.1080/17452759.2024.2396065

VIRTUAL AND PHYSICAL PROTOTYPING
2024, VOL. 19, NO. 1, e2396065 (20 pages)
https://doi.org/10.1080/17452759.2024.2396065

Correlation between microstructural inhomogeneity and architectural design in additively manufactured NiTi shape memory alloys

Zhaorui Yan[a], Jia-Ning Zhu[a], Darren Hartl[b], Ton Riemslag[a], Sean Paul Scott[a], Roumen Petrov[a,c], Marcel Hermans[a], Jovana Jovanova[a] and Vera Popovich[a]

[a]Faculty of Mechanical Engineering, Delft University of Technology, Delft, The Netherlands; [b]Department of Aerospace Engineering, Texas A&M University, College Station, USA; [c]Department of Electromechanical, Systems & Metal Engineering, Ghent University, Ghent, Belgium

ABSTRACT

Additively manufactured Nitinol (NiTi) architectured materials, designed with unit cell architectures, hold promise for customisable applications. However, the common assumption of homogeneity in modeling and additive manufacturing of these architectured materials needs further investigation because geometric-dependent melt pool behaviour results in inhomogeneous microstructure and thermomechanical properties. This study shows that property inhomogeneity at the mesoscale is one reason for pseudo-linear response and partial superelasticity of the fabricated NiTi body-centered cubic (BCC) architectured materials. We modeled using a phenomenological constitutive relation and additively manufactured NiTi architectured materials with varying relative densities. These fabricated samples showed distinct microstructural textures and compositions that affected their local recoverability. The edge effects and laser turn regions were identified as the causes underlying the observed microstructural inhomogeneity. The dimensionless Fourier number is used to describe the transition of printing modes. This study provides valuable information on rigorous experimental/computational consistency in future work.

ARTICLE HISTORY
Received 20 March 2024
Accepted 14 August 2024

KEYWORDS
Additive manufacturing; NiTi; architectured material; microstructure; functionality; numerical model

Introduction

Recent advancements in additive manufacturing (AM) have demonstrated the successful fabrication of NiTi shape memory alloys and their structures, which show excellent functionality such as shape memory effect, superelasticity, damping, and biocompatibility [1–5]. Leveraging the unique properties of NiTi alloys and the design-manufacturing flexibility offered by AM, researchers have developed NiTi architectured materials for a variety of industrial applications, including shock protection [6–8], actuation systems for automotive and aerospace industries [9,10], and patient-specific implants [3,11–13]. However, the specific architectures and dimensions of the unit cell can significantly influence the as-fabricated microstructure and compositional distribution, due to interactions between the powder, melt pool and fabricated geometry of the architectured materials [14,15]. This inhomogeneous microstructure can result in inconsistent thermomechanical properties of the base NiTi, which causes the performance of NiTi architectured materials to deviate from intended designs and properties-relative density relation [16]. Thus, a deeper understanding of the impact of geometric factors of additively manufactured NiTi architectured materials on the melt pool, solidification microstructure, and macroscopic mechanical responses is crucial for developing a reliable design methodology and manufacturing.

In the laser-based AM of bulk samples, the melt pool and microstructure can be controlled by adjusting various process parameters, with a dominant heat dissipation occurring along the building direction (BD). Extensive experiments have demonstrated that superior shape memory effects and superelasticity can be achieved by parameter optimisation, when the melt pool is minimally influenced by geometrical edges [2,17–20]. For instance, Xue et al. [21] fabricated a textured Ni-rich NiTi sample exhibiting a tensile superelasticity of 6%. Zhu et al. [22] achieved unprecedented superelasticity in a Ni-lean Ni (49.4 at.%)-Ti in the ⟨001⟩ textured additively manufactured NiTi. Safdel et al. [19] illustrated the tensile-compression asymmetry of additively manufactured NiTi bulk samples with a

CONTACT Zhaorui Yan Z.Yan-1@tudelft.nl Faculty of Mechanical Engineering, Delft University of Technology, Building 34, Mekelweg 2, 2628 CD Delft, The Netherlands

Supplemental data for this article can be accessed online at https://doi.org/10.1080/17452759.2024.2396065.

⟨001⟩ texture and proposed optimal process parameters to minimise the asymmetry.

In laser powder bed fusion (L-PBF) of metallic architectured materials, the process optimisation strategy aims to achieve geometric features and desirable macroscopic properties [23–25]. However, the L-PBF process often results in inhomogeneous microstructures and varied local mechanical properties due to different heat dissipation from the melt pool to the fabricated structure. Several studies have reported the influence of macroscopic dimensions and unit cell architecture on the microstructure of base materials, focusing primarily on elastoplastic metals such as stainless steel [26,27], Al-based [15,28], Ni-based [29], and Ti-based [30,31] alloys. Johnson et al. reported the elastic stiffness of struts varies from 44 ± 4 MPa to 89 ± 38 MPa using high-energy X-ray diffraction [32]. Elastoplasticity constitutive relations, such as J2 plasticity and Johnson-Cook plasticity are reasonably accurate in the design and model, as elastoplastic behaviours are generally validated across local microstructures. However, this assumption of homogeneity needs further examination for additively manufactured NiTi architectured materials, given that the martensitic transformation and re-orientation are highly sensitive to compositional distribution, texture and precipitates [33–37].

In the modeling of NiTi and other shape memory alloys (SMA) with martensitic transformation, the constitutive models have been significantly developed for conventionally manufactured SMAs [38–40]. These models enable the design and manufacturing of SMA devices with reasonably accurate simulations [39,41–43]. When using the constitutive model in structural analysis, a common calibration approach is based on a one-dimensional reduction of the constitutive model and uniaxial loading tests conducted on wire or bulk samples, often assuming homogeneous and consistent properties across tested samples and other fabricated samples [25,44,45]. In our previous research, we found that the effective transformation stress of architectured materials increases with higher relative density based on this assumption [6]. However, narrow stress hysteresis and partial superplasticity were observed in experiments, as widely reported in the literatures [6,12,13,46]. These experimental findings suggest that the inhomogeneity of base NiTi in additive manufacturing of architectured materials needs reexaminination.

To address this issue in the L-PBF of NiTi architectured materials, it is crucial to investigate the formation of microstructure inhomogeneities [47]. A recent study reported by Jiang et al. [48] illustrated a significant size effect on the microstructure and decrease of martensitic transformation temperatures of thin-wall samples. A different hatching distance was used in this study for the manufacturing of different thin wall samples. Dadbakhsh et al. [49] achieved improved superelastic behaviour by using a combination of high laser power and high scanning speed but the inhomogeneous properties were not fully discussed. For L-PBF of NiTi architectured materials using the same process parameters, the key factor is the geometrically dependent interaction between the melt pool, powder bed and as-fabricated strut of architectured materials. Martin et al. [50] revealed that overheating at laser turn regions leads to increased evaporation of alloying elements due to the changes in scanning speed. Numerous studies, building on the classical Rosenthal solution, have investigated heat transfer in both single-track and bulk manufacturing [51–54]. Given the potential edge effects of struts, it is necessary to analyze the relative measure of the melt pool and geometric dimension, and its correlation to the thermal field during L-PBF of truss-based architectured materials.

In this study, we explained a potential cause for the pseudo-linear response and partial superelasticity observed in NiTi architectured materials. The influence of geometric relative density on the inhomogeneous microstructure and the spatial variation in thermomechanical properties are analyzed, in NiTi architectured materials with a body-centered cubic (BCC) structure and relative densities of 0.1, 0.4, and 0.6. The thermal model with dimensional analysis was conducted to explain the edge effect and transition from strut-based to bulk-based printing mode. The mechanical model with unified constitutive law was developed to predict the impact of inhomogeneous transformation temperatures on the macroscopic response of fabricated NiTi BCC architectured materials.

Geometry and computational models

Conduction-based thermal modeling of melt pool during L-PBF processes

BCC structures with nominal relative densities of 0.02 (extreme condition), 0.05, 0.1, 0.2, 0.3, 0.4, 0.5, and 0.6 were chosen to understand the geometric effect on heat transfer during the L-PBF process. The unit strut, each with respective diameters of 0.24, 0.40, 0.60, 0.84, 1.08, 1.30, 1.50, and 1.70 mm, was calculated using a second-order approximation equation of relative density $\overline{\rho}$ [55],

$$\overline{\rho} = 3\sqrt{3}\pi\left(\frac{R}{l}\right)^2 - 18\sqrt{2}\pi\left(\frac{R}{l}\right)^3, \quad (1)$$

where R and l are the radius and length of the beam.

To understand the geometric effect on the melt pool during L-PBF processes, finite element simulations are carried out using the commercial framework Abaqus/Standard 2019. The multiscale problem in space, between the size of the melt pool and the structure, can lead to a trade-off between solution accuracy and computational time. For this consideration, heat transfer in the beam is modeled using the heat conduction equation [56]:

$$\rho(T)c_p(T)\frac{\partial T}{\partial t} = \nabla \cdot (k(T)\nabla T), \tag{2}$$

where T is the temperature, ρ, c_p and k are the temperature-dependent thermal density, the constant pressure specific heat and conductivity, respectively. The laser beam is modeled using a simple ellipsoid model derived from the double ellipsoid model by Goldak [57]:

$$Q = \frac{2\eta P}{c_1 c_2 c_3 \pi\sqrt{\pi}} \exp\left[-\left(\frac{x_1^2}{c_1^2} + \frac{(x_2 + vt)^2}{c_2^2} + \frac{x_3^2}{c_3^2}\right)\right], \tag{3}$$

where Q is the heat flux density of the laser beam, η is the absorptivity of the material, P is laser power, c_1, c_2 and c_3 are the ellipsoid semi-axis respectively and v is the scanning speed. The laser penetration c_3 is 130 µm and η is 0.50 based on validation experiments.

The adiabatic boundary condition is applied on the edge of the strut due to the weak heat conduction from the as-fabricated structure to the powder [58–60]. The temperature-dependent thermal properties ρ, c_p, and k are provided in Figure S1. The material states (powder and solid) are considered using solution-dependent variables in the UMATHT subroutine [56,61]. More discussion on the thermal properties used in the thermal model is provided in the supplementary documents. Melt pool convection is defined using enhanced thermal conductivity, set to 5 in this work [56]. Heat dissipation due to radiation and convection are considered, using a combined heat transfer coefficient of 20 W/m^2 K [57].

The heat accumulation induced by as-fabricated deposition is treated as residual temperature. It has been reported that residual temperature reaches a steady condition after a few layers of material are deposited, thus residual temperature is modeled using an analytical equation to expedite the computation [62,63]. The initial conditions are set to the residual temperature after the deposition of 50 layers, as given by

$$T_{res}(r, N_A) = T_{in} + \frac{1}{\rho c_p\sqrt{4\pi\cdot\kappa}} \cdot \sum_{N=1}^{N_A} \frac{Q_{1D}}{\sqrt{(N/f)^{n_D}}} \cdot \exp\left(\frac{-f}{N} \cdot \frac{(r - Ns)^2}{4\kappa}\right), \tag{4}$$

where T_{res} is the residual temperature, T_{in} is the initial temperature before processing, Q_{1D} is the one-dimensional heat source, N_A is the number of energy inputs, and f is the frequency of repetitive energy input, κ is the thermal diffusivity, *r-Ns* is the conversion of coordinates for the moving heat source. The constant material properties for this linearised equation such as density, heat capacity and thermal diffusivity are chosen at a temperature close to the melting point [59].

The strut and validation models are discretized using 3D 8-node linear elements (DC3D8R). The powder layer is meshed with an approximate size of 20 µm × 20 µm × 10 µm, while the deposition layer is gradiently meshed from 20 µm × 20 µm × 10 µm to 20 µm × 20 µm × 60 µm. The mesh size is determined to balance mesh convergence, the geometric accuracy of the melt pool, and computational time. After obtaining the numerical results, they were converted to the.vtk (Visualization Toolkit) format and further post-processed using the open-source framework Paraview.

Mechanical models

Mechanical models of uniaxial compression on full samples are developed to understand the influence of inhomogeneous thermomechanical properties on the macroscopic response of the NiTi BCC architectured materials using the commercial framework Abaqus/Standard 2019. Here, the constitutive model of the thermomechanical behaviour of NiTi is recalled [10,40,42]. The total infinitesimal strain is the sum of elastic, thermal and transformation strain:

$$\boldsymbol{\varepsilon} = \mathbf{S}(\xi)\boldsymbol{\sigma} + \boldsymbol{\alpha}(T - T_0) + \boldsymbol{\varepsilon}^t, \tag{5}$$

where $\boldsymbol{\alpha}$ is the thermal expansion tensor, T_0 is a reference temperature, and $\mathbf{S}(\xi)$ is the compliance tensor calculated based on the martensite volume fraction ξ using the rule of mixtures. The evolution equation of transformation strain $\boldsymbol{\varepsilon}^t$ is given by a function of the rate of martensitic volume fraction $\dot{\xi}$ and the transformation direction tensor $\boldsymbol{\Lambda}^t(\boldsymbol{\sigma})$:

$$\dot{\boldsymbol{\varepsilon}}^t = \dot{\xi}\boldsymbol{\Lambda}^t(\boldsymbol{\sigma}). \tag{6}$$

For forward and reverse transformation, the transformation direction tensor is defined as follows:

$$\boldsymbol{\Lambda}^t(\boldsymbol{\sigma}) = \begin{cases} \boldsymbol{\Lambda}^t_{\text{fwd}} = \dfrac{3}{2}H^{cur}(\overline{\sigma})\dfrac{\boldsymbol{\sigma}'}{\overline{\sigma}} & \text{if } \dot{\xi} > 0 \\ \boldsymbol{\Lambda}^t_{\text{rev}} = \dfrac{\boldsymbol{\varepsilon}^{t-r}}{\xi^r} & \text{if } \dot{\xi} < 0 \end{cases}, \tag{7}$$

where $\overline{\sigma}$ is the equivalent stress expressed from von Mises plasticity as $\overline{\sigma} = \sqrt{(3/2)\boldsymbol{\sigma}':\boldsymbol{\sigma}'}$, and $\boldsymbol{\sigma}'$ denotes the deviatoric part of Cauchy stress. $\boldsymbol{\varepsilon}^{t-r}$ and $\xi^r$are the

transformation strain tensor and martensite volume fraction at the reversal of the most recent forward transformation. The magnitude of full transformation $H^{cur}(\overline{\sigma})$ is using a decaying exponential function once the equivalent stress exceeds a critical value $\overline{\sigma}_{crit}$:

$$H^{cur}(\overline{\sigma}) = \begin{cases} H_{\min} & \text{if } \overline{\sigma} \le \overline{\sigma}_{crit} \\ H_{\min} + (H_{sat} - H_{\min})(1 - \exp(-k_t(\overline{\sigma} - \overline{\sigma}_{crit}))) & \text{if } \overline{\sigma} > \overline{\sigma}_{crit} \end{cases}. \tag{8}$$

The transformation function is determined for forward and reverse transformation as

$$\dot{\xi}\Phi^t = 0, \text{with } \Phi^t = \begin{cases} \Phi^t_{\text{fwd}} = \pi^t - Y & \text{if } \dot{\xi} > 0 \\ \Phi^t_{\text{rev}} = -\pi^t - Y & \text{if } \dot{\xi} < 0' \end{cases} \tag{9}$$

where Y is the critical thermodynamic driving force. The thermodynamic driving force for transformation π^t, work conjugate to ξ, is given as

$$\pi^t = \boldsymbol{\sigma}:\boldsymbol{\Lambda}^t + \frac{1}{2}\boldsymbol{\sigma}:\Delta\mathbf{S}\boldsymbol{\sigma} + \rho\Delta s_0 T - \rho\Delta u_0 - f^t(\xi), \tag{10}$$

where the operator Δ denotes the difference in material constant between martensite and austenite (e.g. $\Delta S = S_M - S_A$, and s_0 and u_0) are the specific entropy and specific internal energy at the reference state. In practice, Δs_0 and Δu_0 are defined as model parameters. Finally, $f^t(\xi)$ is the transformation hardening function, which is described as follows:

$$f^t(\xi) = \begin{cases} f^t_{\text{fwd}}(\xi) = \frac{1}{2}a_1(1 + \xi^{n_1} - (1-\xi)^{n_2}) + a_3 & \text{if } \dot{\xi} > 0 \\ f^t_{\text{rev}}(\xi) = \frac{1}{2}a_2(1 + \xi^{n_3} - (1-\xi)^{n_4}) - a_3 & \text{if } \dot{\xi} < 0' \end{cases} \tag{11}$$

where parameters a_1, a_2 and a_3 are computed from material properties and exponents n_1, n_2, n_3 and n_4 are real numbers in the interval (0,1] that govern the 'smoothness' of the transformation curves. The material model above is implemented using the UMAT subroutine with a return mapping algorithm [40]. The calibration of thermomechanical properties of NiTi with homogeneity assumption is shown in Figure S3, Table S1 and early study [6].

The $5 \times 5 \times 5$ unit cells samples with a unit cell size of 4 mm were investigated in numerical models and experiments. The BCC architectured materials are subjected to uniaxial compression between two rigid planes with a frictional coefficient of 0.2. Due to the changes of thermomechanical properties, both the superelasticity and one-way shape memory effect are considered in simulations. The functional response is modeled using displacement loading applied to a rigid plane with the same maximum displacement used in uniaxial compression tests. The geometry is discretized using linear solid element C3D8R with a seed size smaller than 0.25 mm after convergence analysis. The reaction force and displacement of the upper rigid plane are used to compute the engineering stress and strain of the full-tessellated simulations along the loading direction.

Table 1. Geometrical parameters of bulk and BCC architectured samples.

Sample	Nominal relative density (-)	Nominal strut diameter (mm)	As-fabricated strut diameter (mm)
BCC 0.1	0.1	0.6	0.68 ± 0.04
BCC 0.4	0.4	1.3	1.28 ± 0.27
BCC 0.6	0.6	1.7	1.69 ± 0.18

Experimental procedures

Materials and manufacturing

BCC structures of $5 \times 5 \times 5$ cells and cylindrical bulk samples were manufactured by laser powder bed fusion (L-PBF) using an Aconity3D Midi machine equipped with a fiber ytterbium laser (1060 nm wavelength). After reviewing parameter optimizations on bulk samples [64], and high-power manufacturing strategy proposed by Dadbakhsh et al. [49] and Xue et al. [21], all samples were manufactured using a laser power of 400 W, a scanning speed of 1250 mm/s, a hatching space of 120 μm, and a powder thickness of 30 μm. The scanning strategy employed was the stripe scanning strategy, with a rotation of 67.5° between layers. High-purity Argon gas was used as an inert gas to prevent oxidation during the manufacturing process. The feedstock used for the powder bed was commercial $Ni_{51.4}Ti_{48.6}$ powder, which had a spherical shape and D-values of 23 μm (D_{10}), 40 μm (D_{50}), and 67 μm (D_{90}). This powder was fabricated through gas atomisation. Cylindrical bulk samples with a diameter of 13 mm and a height of 20 mm, and BCC structures with nominal relative densities of 0.1, 0.4, and 0.6 were manufactured for microstructural characterisation and mechanical tests (Table 1). The relative density of the manufactured samples is selected based on the relative dimensions between the strut size (refer to Table 1) and the melt pool.

Characterisation and mechanical tests

Cross-sectional samples were obtained by cutting along the macroscopic (110) plane∥ BD, as shown in Figure 1 (a), using Electrical Discharge Machining (EDM). All samples were then ground and mechanically polished using a solution consisting of 70 ml OPS and 30 ml H_2O_2. To recover any polished-induced residual martensite, the polished samples were heated using hot water

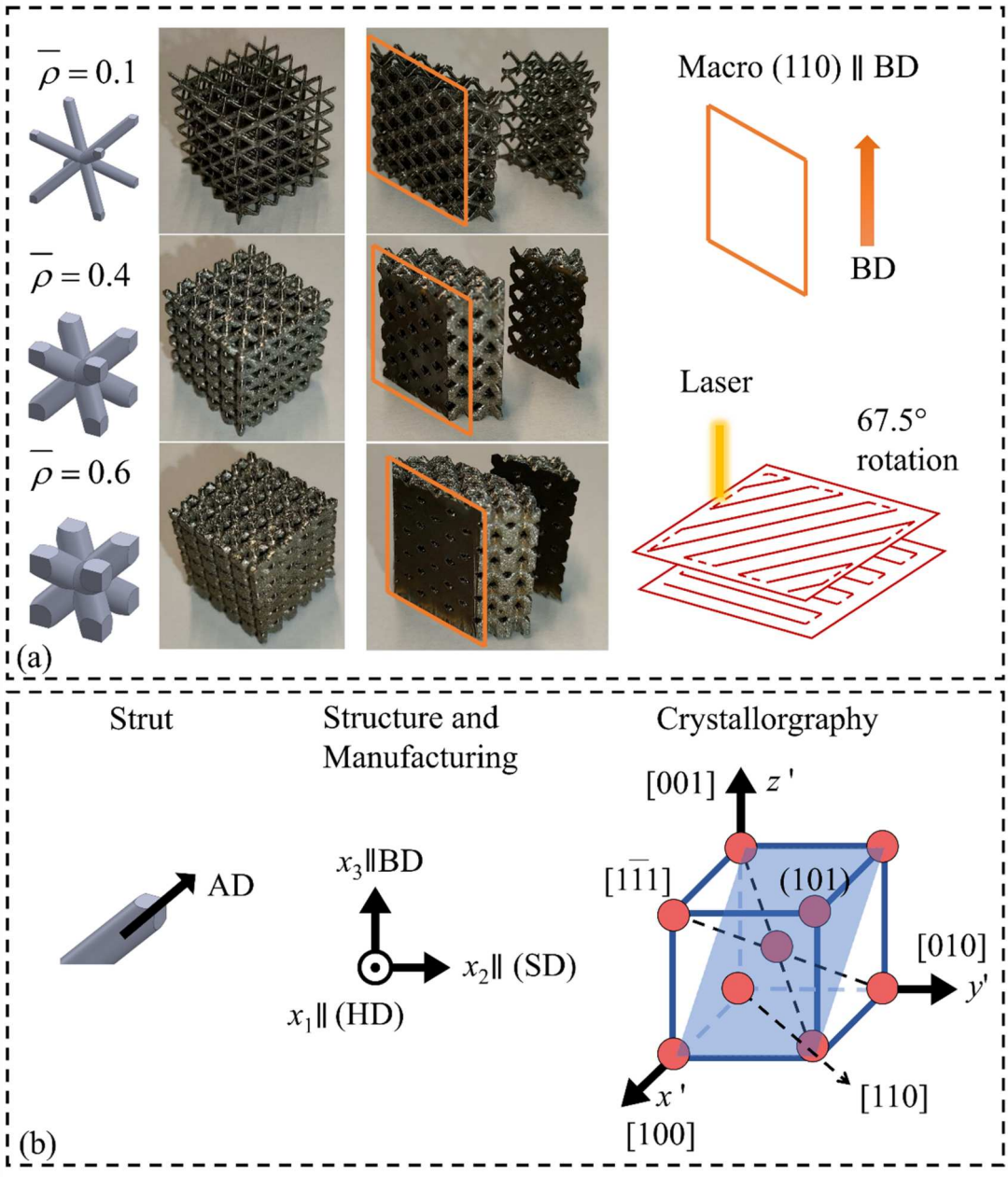

Figure 1. (a) Schematical diagram of macroscopic (110) cutting plane of as-fabricated samples (b) coordinate systems used in the current study.

at a temperature up to 100°C, followed by cooling to room temperature. The images used for thermal model validation and measurement of the laser return region were characterised using scanning electron microscopy (SEM, JSM-IT100). The length of the laser return region was determined by the change of the surface morphology at the laser return region. Texture analysis was conducted using a scanning electron microscopy (SEM, Helios G4) equipped with an electron backscatter diffraction (EBSD) detector with a step size of 2 μm. Grains were characterised using OIM analysis, where grains were considered as ellipses, partitioned with a tolerance angle of 5°. Only grains with more than 30 pixels were considered in the calculation, and those at the edges were excluded from the analysis. Two repetitions of EBSD were performed on each sample for statistical significance. The Phase analysis was carried out using X-ray diffraction (XRD), using a Bruker D8 Advance diffractometer (Cu Ka radiation) with a step size of 0.043° and a counting time of 4 s per step. For measuring the transformation temperatures, Differential scanning calorimetry (DSC, TA Instruments DSC250) was employed at a heating/cooling rate of 10°C/min over a temperature range of −70 to +150°C.

The cyclic compressive tests on NiTi BCC architectured materials were conducted using universal mechanical tests (Zwick Z100) with a heating chamber at a constant temperature of 54°C. Displacement and engineering strain of architectured materials were measured using a contact extensometer. Cyclic compression tests contain 10 cycles, corresponding to the number of stabilised cycle used in calibration experiments. Displacement-controlled loading was applied, with a maximum displacement of 0.8 mm for the BCC 0.1 sample and 0.7 mm for the BCC 0.4 and 0.6 samples, at a strain rate of $5 \times 10{-}4\ s^{-1}$.

To evaluate the local mechanical response, instrumented indentation was conducted using a Zwick ZHU2.5 at room temperature. A spherical ball indenter with a diameter of 0.5 mm was used to avoid plastic deformation. The indention was controlled to produce a constant increment of 0.1 N/s until reaching the maximum force of 20 N. The hold time at the maximum force was set at 10 s.

In summarising the methodology, three coordinate systems are used in this study, as depicted in Figure 1 (b). The first coordinate system is the cylindrical coordinate system used for the strut at the mesoscale, specifically referring to the axial direction (AD) of the strut. The second one is the Cartesian coordinate system employed in L-PBF, corresponding to the building direction (BD), scanning direction (SD), and hatching direction (HD) of the laser head. The Cartesian coordinate system x_1, x_2 and x_3 is used in the numerical model. The last coordinate system is the Cartesian coordinate system utilised in texture analysis at the microscale, referencing Miller indices in crystallography.

Results

Melt pool profiles

The melt pool profiles for the parameters used in the current study are shown in Figure 2 (a) and Figure S2. The melt pool depth (155 ± 10 μm) surpasses multiple layer thickness (30 μm), resulting in remelting and re-solidification of as-fabricated material (Figure 2(b)). To ensure the accuracy of the heat source and UMATHT subroutine, the validation of the thermal model is performed using the geometrical dimensions of the melt pool. As illustrated in Figure 2 (b) and (c), the melt pool profile is consistent with the prediction of the simulation. The predicted width of the melt pool is closely validated by the experimental results. The simulated depth of the melt pool is 141 μm, 9% smaller than the average value in experiments (Figure 2 (a)).

The validated simulations were extended to thermal simulation for manufacturing BCC structures as shown in Figure 3 (a). The influence of strut dimensions on heat flux is illustrated in Figure 3 (b). In the BCC structure with low density (nominal relative density of 0.02 and 0.1), the heat dissipation is restricted by the low conductivity between the solid strut and the powder bed [60]. The small strut dimension also constrains the extension of the melt pool in the scanning direction, resulting in a puddle-like shape of the melt pool. Consequently, the temperature gradient and high conductivity in the as-fabricated strut direct the dominant heat flow close to the axial direction of the strut. Conversely, in BCC structures with higher relative densities (0.4 and 0.6), the dimple-like melt pool extends into a long and flat morphology due to the increased scanning distance. The effect of low conductivity of powder on the heat transfer in the strut is attenuated. Heat transfer in the manufacturing of a thick strut can be approximated to that of a bulk sample, with the dominant direction of heat flux at the melt pool bottom close to the building direction [51].

Dependence of microstructures on geometrical dimensions

As shown in the XRD pattern (Figure 4), the B2 parent phase with a BCC crystal structure is the predominant phase for all BCC samples at room temperature. The BCC samples exhibit three strong diffraction peaks corresponding to (110), (200) and (211) Miller indices. Variations of peaks among samples with different relative densities are attributed to the different sampling areas of diffraction beam projecting on the samples.

The homogeneous microstructure and texture of the bulk sample were analyzed using EBSD, as illustrated in Figure S4. Inverse Pole Figures (IPF) for the building direction (IPF-BD), showing the sample cross-sections perpendicular and parallel to the BD, are presented in Figure S4 (a) and (b) with a colormap corresponding to the BD in the manufacturing coordinate system. It was observed that most grains exhibit a strong ⟨001⟩ orientation aligned with the BD, and columnar grains epitaxially grow along the BD. The corresponding pole figure (PF) further confirms these results as shown in Figure S4 (c) and (d). The highly ⟨001⟩ textured microstructure is attributed to the vertical maximum heat flux direction in the bulk sample and the insignificant edge effect, consistent with findings reported in previous studies [19,34]. Given the homogeneous microstructure at the sample scale, homogeneous mechanical properties were achieved across the bulk sample.

Texture analysis was conducted using EBSD on selected areas of BCC samples with relative densities of

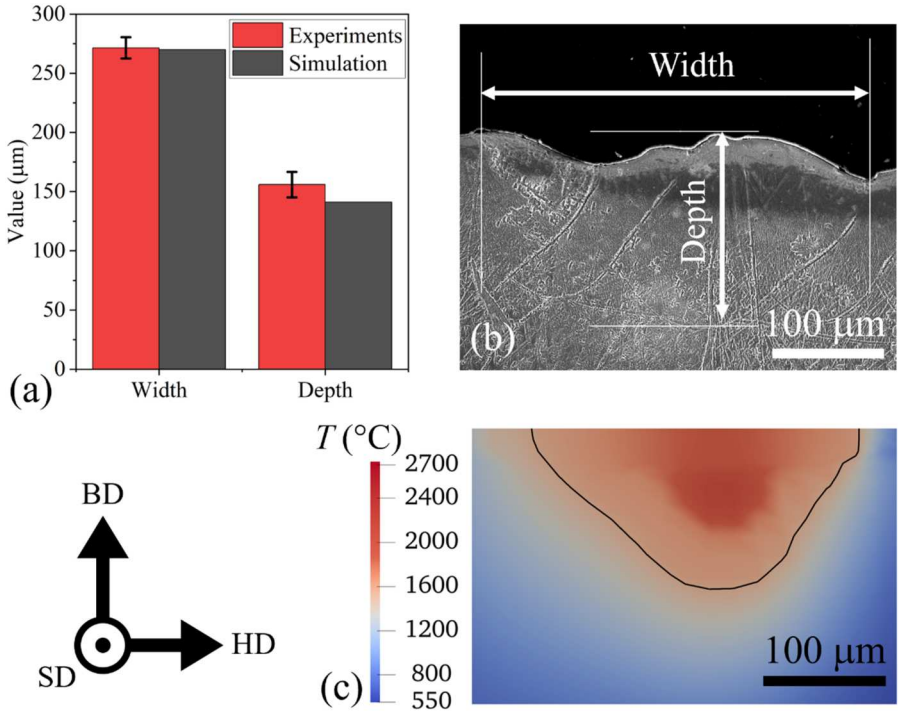

Figure 2. (a) Validation of thermal simulation by comparing the width and depth of the melt pool, (b) experimental melt pool profile, and (c) corresponding melt pool profile from thermal simulation.

0.1, 0.4, and 0.6, as shown in Figure 5 (a). Three distinct textures are observed in three samples fabricated using the same process parameters. Figure 5 (b) presents an IPF of the macroscopic (110) cross-section for sample BCC 0.1, using a colour map corresponding to the axial direction (IPF-AD). In this sample, cellular grains are observed in the lower portion of the strut, while columnar grains dominate the central and upper regions. The elongation of the columnar grains in the upper area was promoted along the axial direction, gradually transitioning towards the vertical direction at the center of the strut. This columnar area exhibits a distinct texture parallel to the AD. Figure 5 (f) shows the corresponding Pole Figure (PF) for the same region, confirming the texture orientation observed in the IPF-AD.

For the sample BCC 0.4, Figure 5 (c) illustrates the IPF of the strut with the colormap corresponding to the BD (IPF-BD). In the central and bottom regions, a strong ⟨001⟩ // BD texture is observed, which is further confirmed in the corresponding PF (Figure 5(f)). In the upper portion of the strut, columnar grains with shorter elongation were observed, and the growth direction shifted from the building direction to the strut AD. At the top area of the strut, columnar grains with less elongation are observed, and the elongation of the grains deviates from BD to AD of the strut. Figure 5 (d) and (e) illustrate the IPF of the macroscopic ⟨110⟩ cross-section of the strut and node in the sample BCC 0.6, with colormap aligned with the BD (IPF-BD). Coarse columnar grains are observed in the node area, characterised by elongation along the building direction. However, a comparably weaker texture is observed, differing from the results of BCC 0.4 and 0.1 samples.

The grain morphology was defined as ellipses with major axis and minor axis for statistical analysis. The effect of relative density on the major axis and minor axis is presented in Figure S5. The EBSD analyses were performed twice on samples with identical relative density, and the results were subsequently combined. These replicates were adopted to encompass a sufficient number of grains within the statistical analysis. In total, the quantitative analysis comprised 915, 1355, and 2773 grains for the BCC 0.1, BCC 0.4, and BCC 0.6 samples, respectively. The averaged fraction corresponding to these morphology parameters is calculated, in the figure legend. The largest average major axis of the elongated grains was observed in the BCC 0.1 samples (36.5 μm) (Figure S5 (a)). The minor axis of the grains showed a consistent average value across the samples, which slightly increased from 7.2 to 7.9 μm (Figure S5 (b)).

Phase transformation behaviour

EDS was conducted on seven different locations in samples with two replicates for statistical significance,

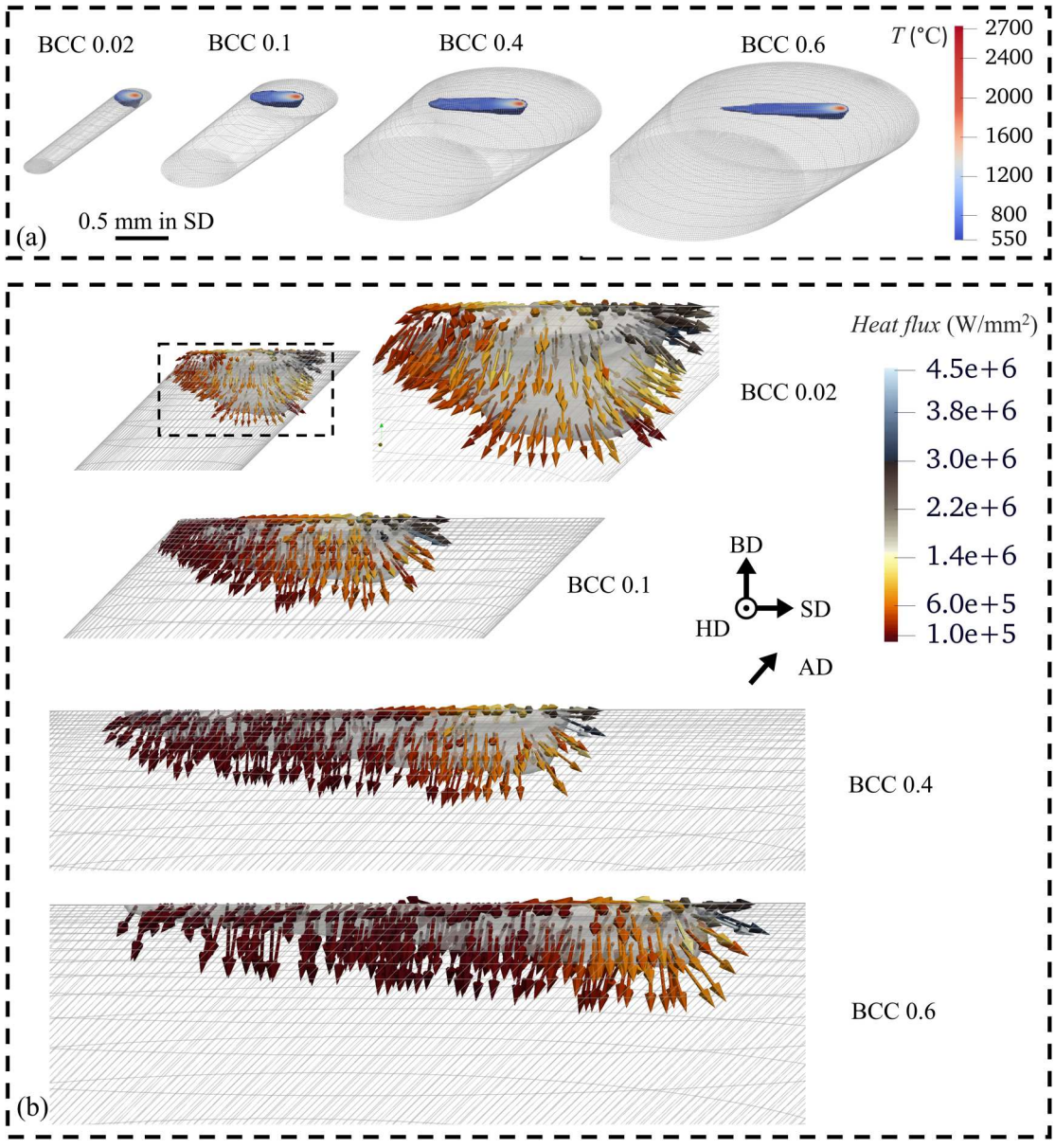

Figure 3. (a) Melt pool profile and (b) heat flow at the solid-liquid zone of melt pool during L-PBF of BCC architectured materials with the relative density of 0.02 (an extreme case), 0.1, 0.4, and 0.6.

and the mean and standard deviation of the measurements are illustrated in Figure 6 (a). The mean Ni content increases with the increase of relative density. The variability in Ni content is related to the occurrence of Ni evaporation during the L-PBF process.

The DSC curves of BCC architectured materials after 4 cycles are shown in Figure 6 (b). The corresponding transformation temperatures (martensite start temperature M_s, martensite finish temperature M_f, austenite start temperature A_s and austenite finish temperature A_f) are determined using tangent lines, as shown in Table 2. All as-fabricated BCC architectured material samples underwent single B2 to B19′ transformation during cooling, and reverse transformation during heating. With the increase of relative density from 0.1 to 0.6, the span of the transformation temperature range (A_f – M_f) decreased, and the peaks became sharper. BCC 0.6 sample exhibited the lowest A_f of 35°C.

The location dependence of recoverability for BCC 0.1, BCC 0.4 and BCC 0.6 samples at room temperature is illustrated in Figure 7. The indentation force-depth responses from instrumented indentation are illustrated in Figure S6. The BCC 0.6 sample exhibits on average higher recoverability under instrumented indentation with a maximum force of 20 N. This higher recoverability at room temperature could be attributed to the lowest

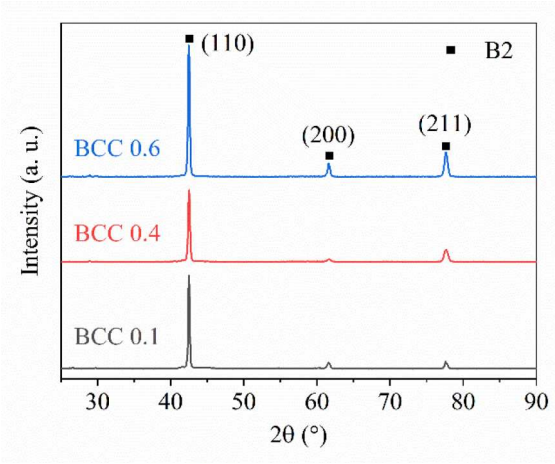

Figure 4. XRD patterns of BCC 0.1, 0.4 and 0.6 NiTi samples at room temperature.

austenite finish temperature (A_f) in the BCC 0.6 sample. The BCC 0.1 and BCC 0.4 samples showed a larger deviation in recoverability at room temperature, mainly due to the wider span of transformation temperatures as shown in Figure 6 (b). It has been reported that an increase of 0.1 at.% Ni could decrease transformation temperatures by approximately 20°C for Ni-rich NiTi [65,66]. A higher Ni content in the BCC 0.6 sample decreased the A_f to approximately 35°C, enabling greater recoverability under indentation at room temperature.

Discussion

Thermal effects on grain size and morphology

The inhomogeneity was observed in three BCC samples with different relative densities, and the formation mechanisms of this unexpected inhomogeneity are discussed. As shown in Figure 5, grain morphology varies with the relative density of the BCC architectured materials, even when using the same process parameters. Grain morphology is controlled by temperature gradient G and solidification rate R_s, as proposed by Güaumann et al. [67]. For cases of high temperature gradient in the L-PBF process, the columnar to equiaxed transition is given as follows [67]:

$$\frac{G^n}{R_s} = a\left\{\sqrt[3]{\frac{-4\pi N_0}{3\ln[1-\varphi]}} \times \frac{1}{n+1}\right\}^n, \tag{12}$$

where $a = 1.25 \times 10^6$ ($K^{3.4}$/m·s) and $n = 3.4$ are material-dependent constants, $N_0 = 2 \times 10^{15}$ m^{-3} is the nuclei density and $\varphi = 0.05$ is a grain morphology factor, which was calibrated in our early studies [22]. As shown in Figure 8 (a), the G-R_s area in the equiaxed region corresponds to the upper region of the melt pool, which is subjected to remelting by successive layers. The area of G-R_s in the central and bottom regions promotes the formation of columnar grains at the bottom area of the melt pool. The columnar grains elongated along the maximum heat flux direction, which can vary from the BD direction to the AD of the strut with the increasing edge effect (Figure 3). Hence, considering the epitaxial growth of columnar grains and the spatiotemporal variation of the direction of the temperature gradient at the solid–liquid interface, the elongation direction of columnar grains in BCC architectured materials with different relative density deviates from building direction to the axial direction of the strut.

Edge effect

As strut dimensions decrease in the L-PBF process using consistent process parameters, the edge effect becomes more pronounced. The structural parameters are provided in Figure S7 and Table S2. An extreme case is shown in Figure 3(b), Figure 9 (b), and (c) for BCC structure with a relative density of 0.02, in which the melt pool occupies the entire cross-section of a unit strut. The temperature history of the central point of the strut during the laser scanning is shown in Figure 9 (b). For low-density BCC structures, the extension and movement of the melt pool along the scanning direction are limited by the strut's dimensions, keeping the central point molten even after one scanning finish. Consequently, the steady state of the moving melt pool cannot be achieved. Conversely, for a BCC structure with a relative density above 0.2, the melt pool progresses along the scanning direction, allowing the central point to begin solidifying once laser scanning ends, as shown in Figure 9(c).

The evolution of the melt pool is influenced by process parameters, scanning strategy, and geometrical parameters as shown in our simulations. To evaluate the edge effect for L-PBF of truss-based architectured materials, we applied the Fourier number (Fo) to analyze it in the scanning direction [53]:

$$Fo = \frac{\kappa\tau}{\delta^2} = \frac{\kappa}{v\delta}, \tag{13}$$

where δ is the characteristic length, which is defined by the characteristic length of the melt pool. κ_τ is the thermal diffusivity of NiTi and τ is the characteristic time. Due to the change in melt pool morphology with different scanning lengths in different layers, the characteristic length of the melt pool is calculated as half the track that was scanned. The Fourier number describes

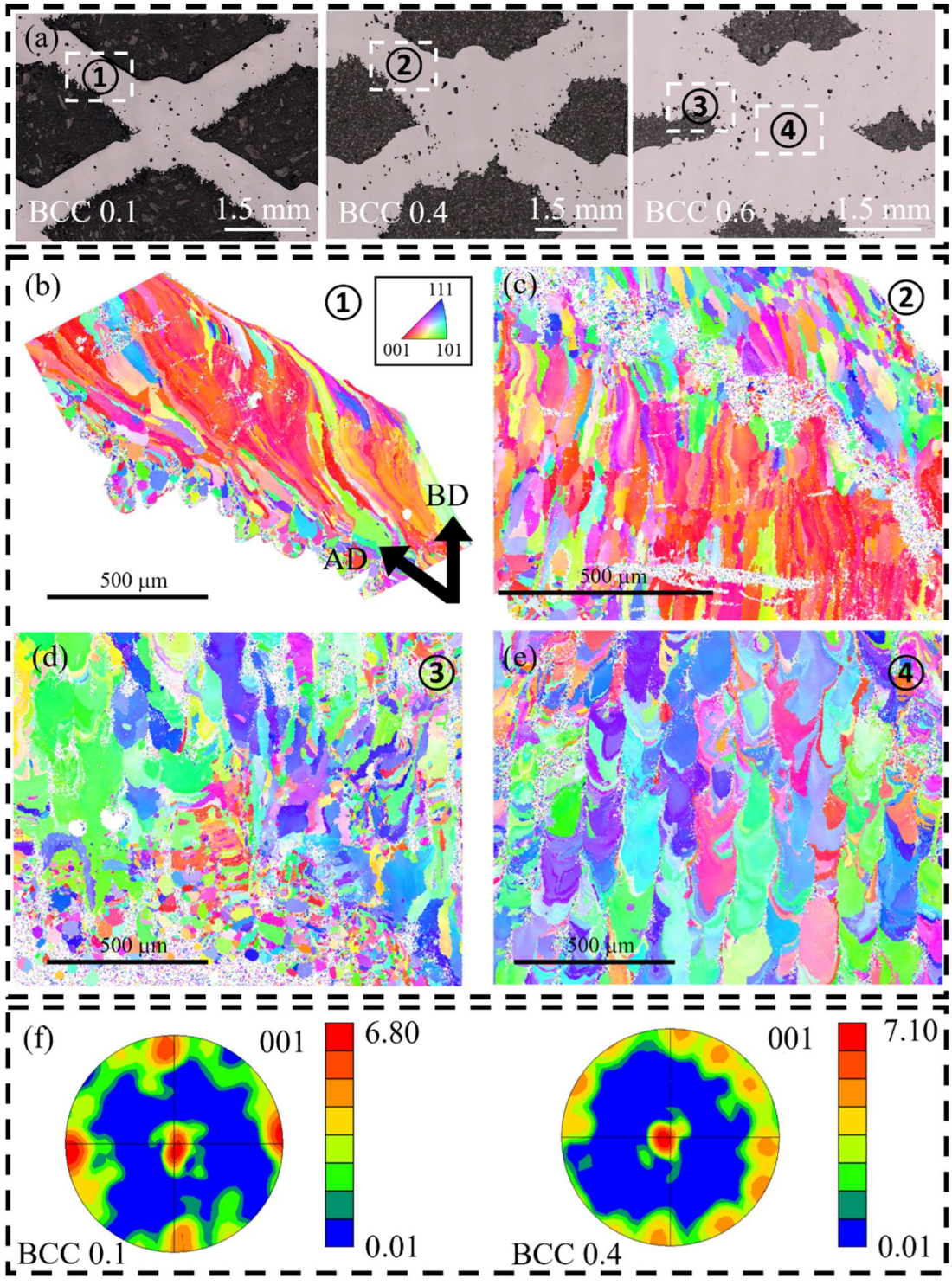

Figure 5. (a) Selected areas of BCC samples with relative densities of 0.1, 0.4, and 0.6. (b) Inverse Pole Figure (IPF) of the macroscopic cross-section for the BCC 0.1 sample. (c) IPF of the strut for the BCC 0.4 sample. (d, e) IPF of the macroscopic cross-section of the strut and node for the BCC 0.6 sample. (f) Corresponding Pole Figure (PF) for the BCC 0.1 and 0.4 samples.

the change in thermal dissipation along the scanning direction.

As shown in Figure 9 (d), the dimensional analysis shows how *Fo* varies with relative density and non-dimensional heat input, due to the combined influence of process parameters and geometrical parameters during L-PBF process. Considering the process parameters used in our experiments, the variation of *Fo* with relative density is shown in Figure 9 (e). For BCC structures with a relative density higher than 0.3, *Fo* remains relatively constant, suggesting a stable relationship between heat input and heat

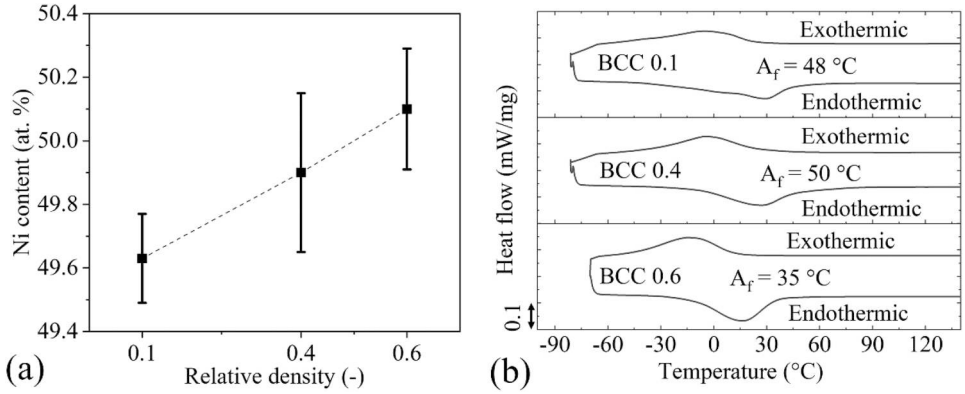

Figure 6. Ni content from (a) EDS and (b) DSC results of the BCC architectured materials with relative densities of 0.1, 0.4 and 0.6.

Table 2. Martensitic transformation temperatures for BCC architectured materials with relative densities of 0.1, 0.4 and 0.6.

Sample	M_s (°C)	M_f (°C)	A_s (°C)	A_f (°C)
BCC 0.1	24	−63	−42	48
BCC 0.4	28	−34	−9	50
BCC 0.6	12	−42	−12	35

dissipation. The printing process can be defined as a bulk-based mode. Conversely, for a BCC structure with a relative density of less than 0.3, the edge effect becomes pronounced, and *Fo* increases with the decrease of relative density, indicating a transition to a strut-based printing mode.

Laser turn region

Fourier number provides a heat conduction-based insight into the geometric effect on the melt pool and the evolution of microstructure. Another mechanism related to geometrical dependence is the overheat at the laser turn region during the L-PBF process. Recent studies reported that acceleration/deceleration at laser start/end points can result in overheat and unexpected defects during laser-based welding and additive manufacturing. In-situ observations and multi-physics simulations have shown that overheat at the laser turn region results in increased metal evaporation and collapse of the melt pool surface [68,69]. For the L-PBF of bulk samples, overheat at the laser turn region is insignificant to the properties because the relative size between laser turn region and the sample is small. However, the impact of the laser turn region becomes more pronounced when the size of the geometry is reduced to the same scale as the laser turn region (Figure 10 (a)).

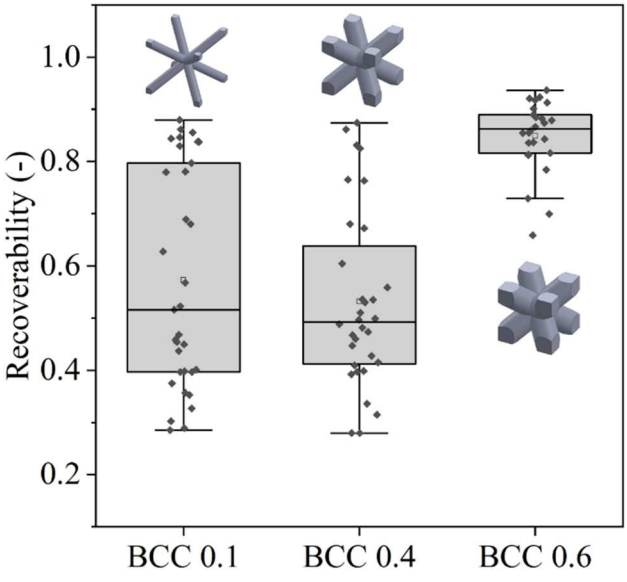

Figure 7. Recoverability in the instrumented indentation of BCC 0.1, 0.4 and 0.6 samples, including statistical mean, median and range.

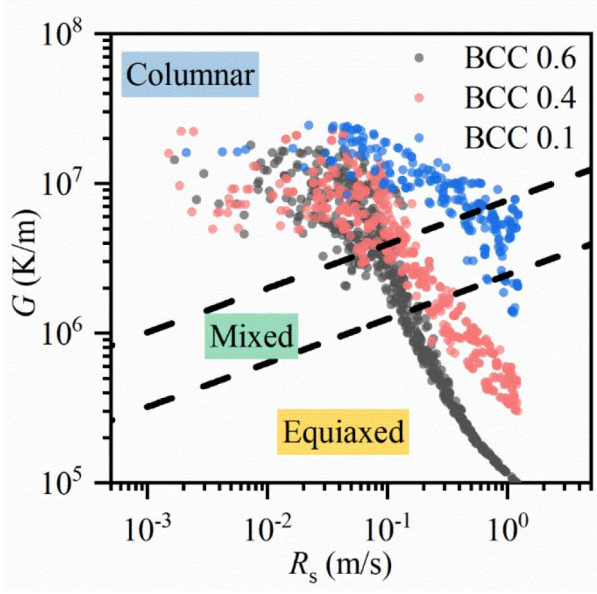

Figure 8. (a) Columnar to equiaxed transition of L-PBF NiTi, where G is the temperature gradient and R_s is the solidification rate.

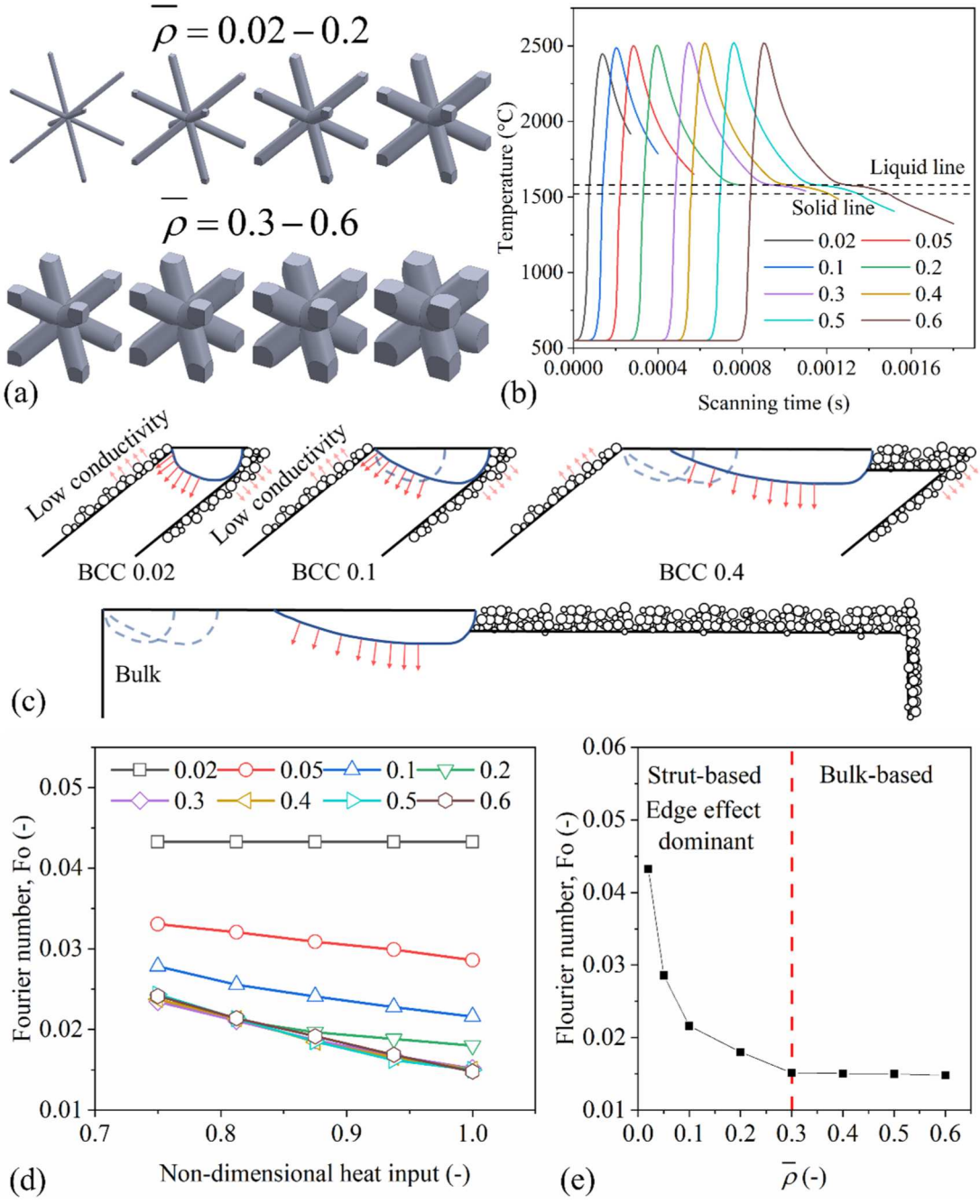

Figure 9. Edge effect in L-PBF of NiTi BCC architectured materials: (a) CAD model of unit cells, (b) temperature history at the central point of the strut, (c) schematic diagram of edge effect, (d) the effect of non-dimensional heat input on the Fourier number, and (e) The effect of relative density of Fourier number for the parameters used in the current study.

As shown in Figure 10 (b), the laser turn region leads to a transition in the surface morphology of the fabricated layer. The average length, measured by an average across twelve scanning tracks, is 636 ± 38 μm for one endpoint of a scanning track (Figure 10 (c)). Overheat at the turn point region leads to the over-evaporation of Ni in a low-density structure (Figure 6 (a)), contributing to an increased A_f of 48°C in sample BCC 0.1 and 50°C in sample BCC 0.4. This observation explains the low A_f of 35°C and an average high indentation recoverability of 84% in sample BCC 0.6 (Figure 7). The significance of the laser turn region is influenced by the different relative lengths between the laser turn region and scanning length. When the scanning length is less than twice the length of the turning region, the overheat region mainly occupies the printing scanning track. Decreased laser power and adaptive control of heat input can be applied to improve the consistency of base NiTi properties.

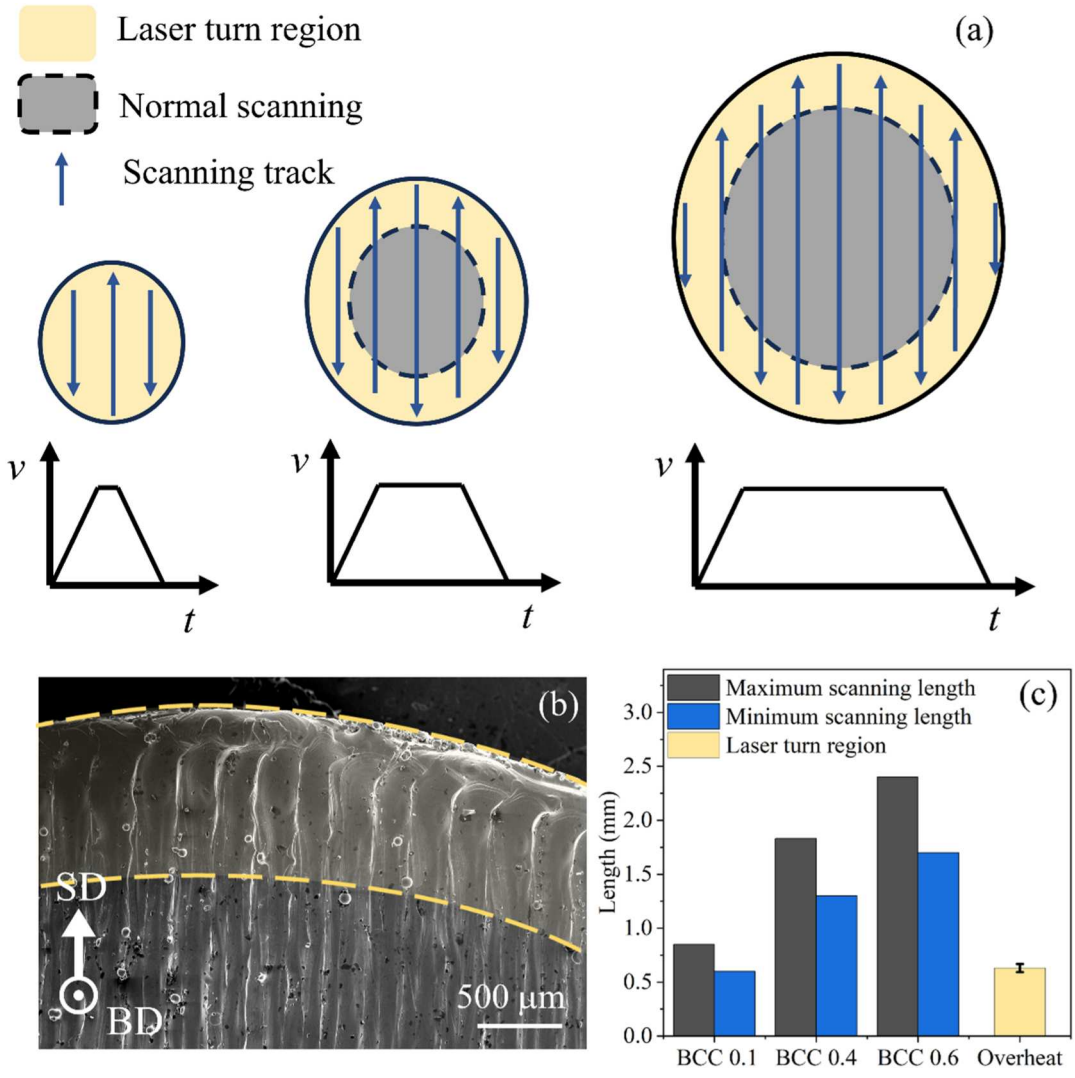

Figure 10. Representation of the laser turn region: (a) schematical diagram (b) SEM picture, and (c) the comparison of scanning length and length of laser turn region.

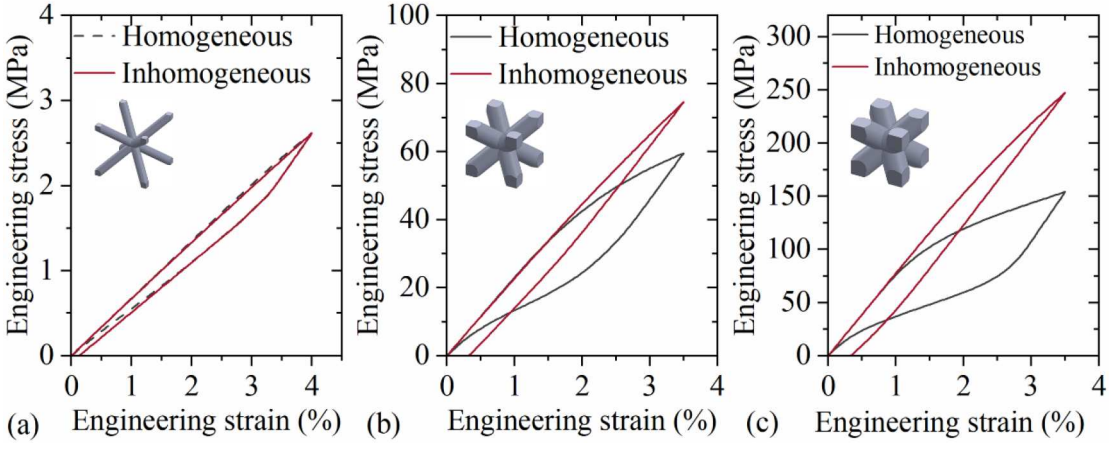

Figure 11. Engineering stress-strain response of NiTi architectured materials with inhomogeneous and homogeneous martensitic transformation temperatures: (a) BCC 0.1, (b) BCC 0.4, and (c) BCC 0.6.

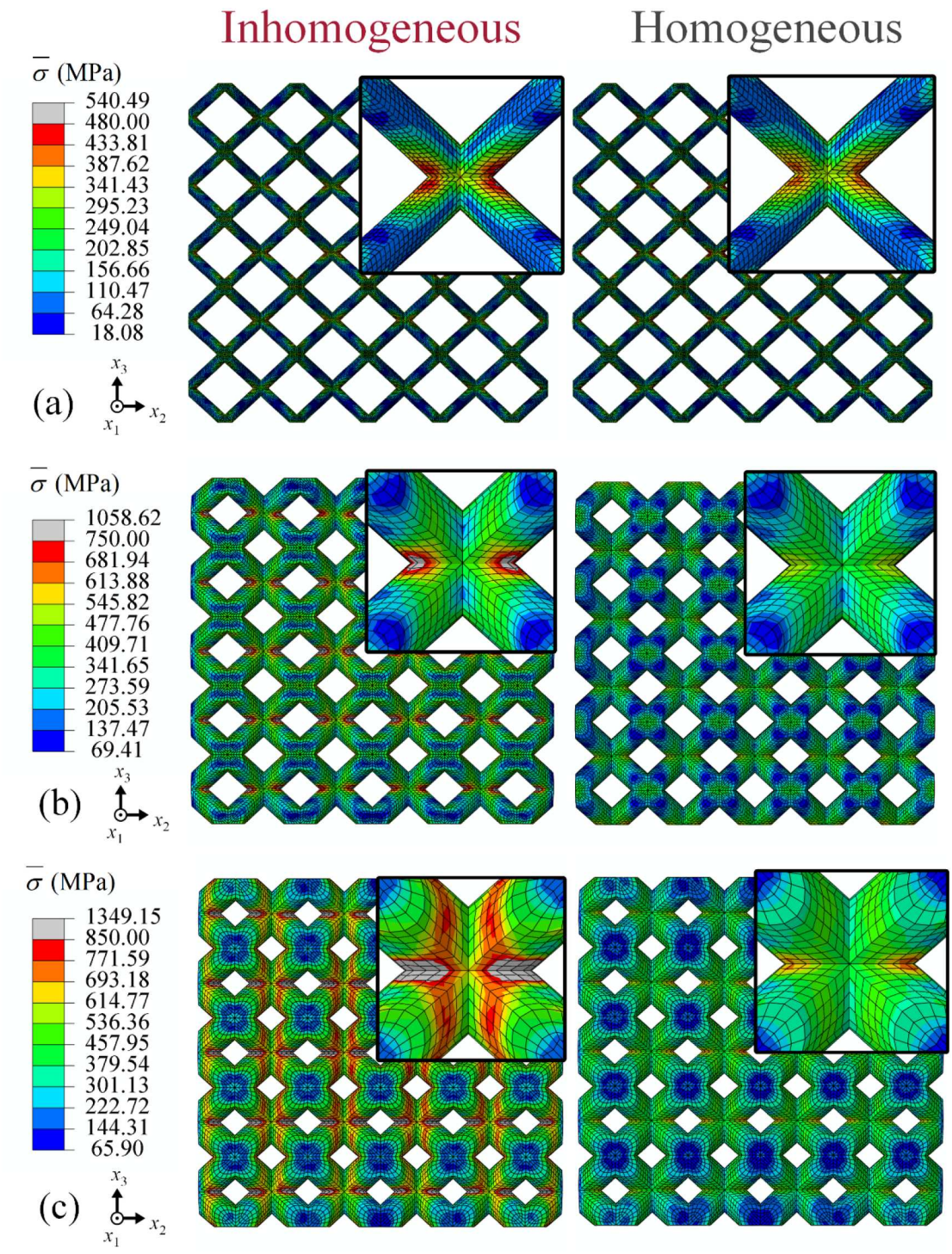

Figure 12. Contour plots of equivalent (von Mises) stress resulting from the inhomogeneous and homogeneous martensitic transformation temperatures in (a) BCC 0.1, (b) BCC 0.4, and (c) BCC 0.6 samples under maximum loading.

Influence of inhomogeneous thermomechanical properties on macroscopic structural response

The significance of inhomogeneous microstructure and thermomechanical properties has been underestimated in previous studies due to limited testing methods [6]. To better understanding this effect, we evaluate the influence of changing transformation temperatures on the macroscopic stress and strain response of BCC architectured materials. In the absence of sufficient experimental data, we first assume that global changes in transformation temperatures are inhomogeneous and

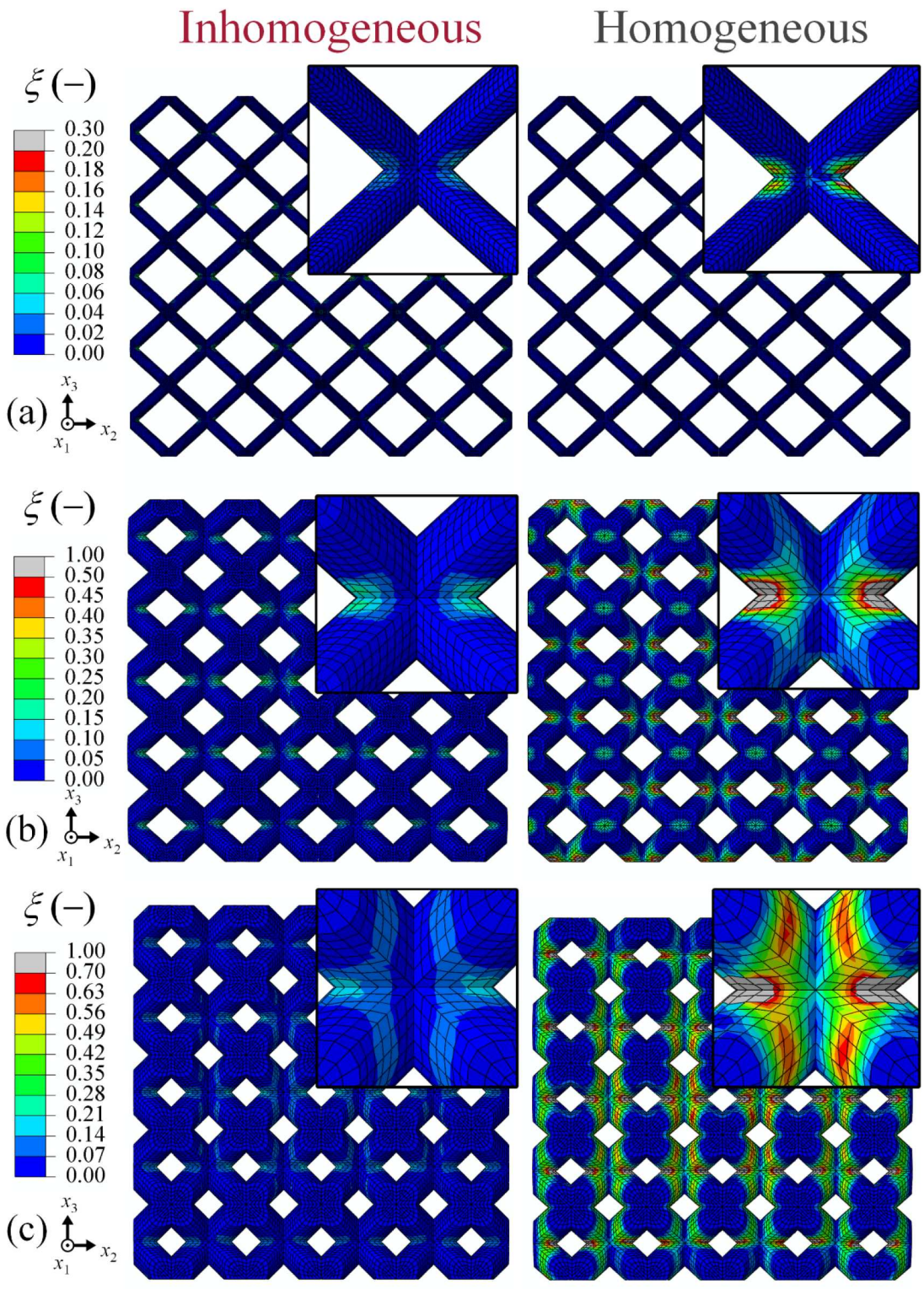

Figure 13. Contour plots of martensitic volume fraction resulting from the inhomogeneous and homogeneous martensitic transformation temperatures in (a) BCC 0.1, (b) BCC 0.4 and (c) BCC 0.6 samples under maximum loading.

follow a multivariate Gaussian distribution:

$$M_s = M_{s0} + \Delta M_s \prod_1^3 \frac{1}{\sigma_i\sqrt{2\pi}} \exp\left[-\frac{(x_i-\mu_i)^2}{\sigma_i^2}\right], \quad (14a)$$

$$M_f = M_{f0} + \Delta M_f \prod_1^3 \frac{1}{\sigma_i\sqrt{2\pi}} \exp\left[-\frac{(x_i-\mu_i)^2}{\sigma_i^2}\right], \quad (14b)$$

$$A_s = A_{s0} + \Delta A_s \prod_1^3 \frac{1}{\sigma_i\sqrt{2\pi}} \exp\left[-\frac{(x_i-\mu_i)^2}{\sigma_i^2}\right], \quad (14c)$$

$$A_f = A_{f0} + \Delta A_f \prod_1^3 \frac{1}{\sigma_i\sqrt{2\pi}} \exp\left[-\frac{(x_i-\mu_i)^2}{\sigma_i^2}\right]. \quad (14d)$$

where M_{s0}, M_{f0}, A_{s0}, and A_{f0} are the calibrated transformation temperatures obtained using DSC under the assumption of homogeneity. ΔM_s, ΔM_f, ΔA_s, and ΔA_f are the differences in transformation temperatures, used to evaluate the global inhomogeneity, which is estimated from DSC curves. The inhomogeneous transformation temperatures are spatially distributed in a global coordinate system that coincides with the manufacturing coordinate system, represented by variables COORD in subroutine UMAT. Future work will extend these efforts to consider the complete heterogeneous assignment of thermomechanical properties.

The calibration is shown in Figure S3 under the assumption of homogeneity and consistency. The transformation temperatures were derived from DSC tests performed on regions from each of the three fabricated BCC lattices (Table 2). The inhomogeneity is estimated from differences in transformation temperatures, which are 30°C for BCC 0.1 and BCC 0.4 samples, and 10°C for BCC 0.6 samples. The response of the printed samples is predicted at an ambient temperature of 54°C, consistent with the conditions of the uniaxial compression tests.

The numerical study in Figures 11–13 and experimental data in Figure 14 show that the inhomogeneous transformation temperatures in BCC samples lead to a pseudo-linear behaviour and a narrow hysteresis across all samples. The expected effective transformation stress for NiTi architectured material is not obviously observed in Figures 11 and 14 [6]. Only partial superelasticity is achieved due to a partial martensitic transformation or reorientation as shown in Figure 13. Higher equivalent stress and lower martensitic fraction are observed in all BCC samples with inhomogeneous transformation temperatures.

The numerical and experimental results suggest that both unit cell design and local thermomechanical properties contribute to macroscopic deformation recoverability, as shown in Figures 12 and 13. The BCC 0.6 sample, which has smaller transformation temperature differences of 10°C, shows low recoverable deformation due to the high structural stiffness, despite a higher reverse martensitic transformation of the base NiTi (Figures 12(c) and 13(c)). Conversely, the BCC 0.1 sample, with a larger transformation temperature difference of 30°C, exhibits larger deformation recoverability due to its structural compliance, while martensite volume fraction is relatively low due to inhomogeneous transformation temperatures (Figures 11(a), 13(a) and 14(a)). Thus, macroscopic compression on architectured materials cannot fully reflect the properties of base NiTi without assuming homogeneity and consistency.

From the above computational and experimental study, one can observe the strong impact of inhomogeneous transformation temperatures on macroscopic mechanical response. However, the transformation temperatures assigned to each of the three structural forms were taken from sample-specific DSC experiments with an effective resolution of 10 mm^2. The discussion of Section 4.3 above implies a possible variation in properties throughout the samples (e.g. due to the laser turn region, etc.) at the length scale of 500 μm. The corresponding sample errors cannot be completely eliminated due to their high inhomogeneity. Therefore, we do not expect the computational predictions in Figures 11–13 to be fully accurate.

The observed narrow hysteresis and partial superelasticity in NiTi architectured materials are likely attributed

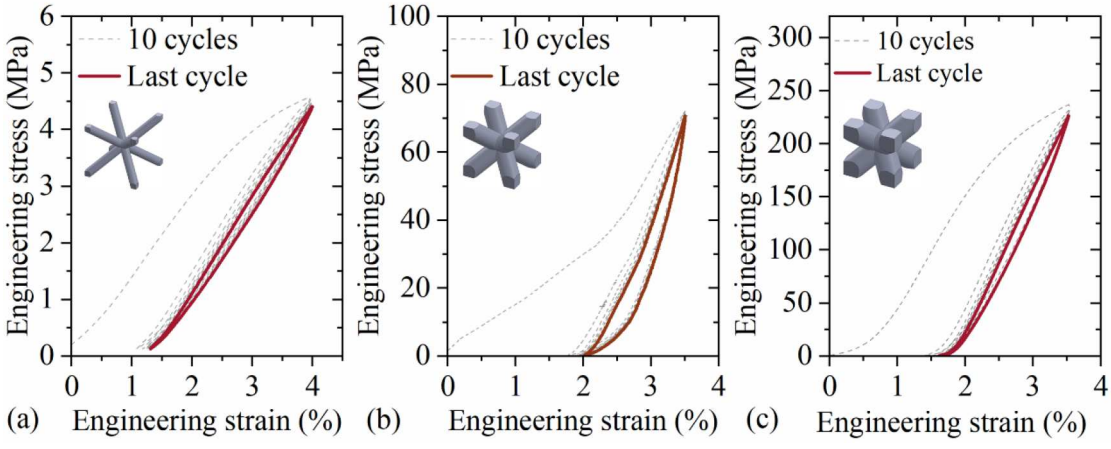

Figure 14. Cyclic compression tests on fabricated BCC architectured materials at 54°C: (a) BCC 0.1, (b) BCC 0.4, and (c) BCC 0.6 samples.

to an inhomogeneous microstructure and spatial variations in properties. While macroscopic compression tests provide valuable trends, they do not confirm that the functionality of the as-fabricated samples aligns with the design objective. This motivates a more rigorous experimental/computational study regarding the specifics of process-induced material heterogeneity in future works.

Conclusions

In the present study, we investigate the inhomogeneity phenomenon in NiTi architectured materials. The influence of relative density on microstructure, local indentation response, and the macroscopic thermomechanical response of as-fabricated body-centered cubic (BCC) structures are discussed. The main findings can be summarised as follows:

(1) The thermomechanical response of NiTi BCC architectured materials is modeled using a phenomenological constitutive model of shape memory alloys. The highly inhomogeneous martensitic transformation temperatures at the mesoscale could lead to a pseudo-linear response and narrow stress hysteresis. The partial superelasticity in NiTi architectured materials is related to microstructure and thermomechanical properties inhomogeneity at the mesoscale.
(2) In low-density, bending-dominated structures, deformation recoverability is jointly attributed to both structural compliance and the recoverable strain of NiTi. The compliance of low-density BCC structures enhances the overall deformation recoverability when superelasticity of the base NiTi is suppressed.
(3) Strut dimensions of architectured materials significantly influence the interaction between the powder bed, melt pool, and as-fabricated layers during the L-PBF process. Short scanning tracks and the low conductivity of the powder bed collectively limit the extension of the melt pool along the scanning direction. Changes in the dominant heat flux direction from axial to building directions influence the growth of columnar grains and textures. This results in distinct textures across the three fabricated BCC samples, varying with strut size.
(4) Excessive evaporation of Ni content occurs during printing, becoming more pronounced when geometrical dimensions are reduced to the scale of the laser turn region. In instrumented indentation, the BCC 0.6 sample shows the highest recoverability (84% at room temperature) due to lower martensite finish temperature A_f.
(5) The edge effect of the strut during L-PBF is clarified using dimensional analysis. The transition from strut-based to bulk-based printing modes is defined using a dimensionless Fourier number.

Acknowledgements

Zhaorui Yan wishes to thank the China Scholarship Council (CSC) for the financial support. The valuable suggestions and discussions about the thermal model from Yang Yang, Can Ayas, Amin Ebrahimi and Xiaohui Liang are greatly acknowledged. The authors are grateful to Evgenii Borisov (from Peter the Great Saint-Petersburg Polytechnic University) for support in the additive manufacturing of lattice samples. The authors also would like to acknowledge the help from Durga Mainali, Kees Kwakernaak, Richard Huizenga and Roy Awater for materials preparation, characterisation and analysis.

Disclosure statement

No potential conflict of interest was reported by the author(s).

Funding

This work was supported by China Scholarship Council: [Grant Number].

Data availability statement

The data that support the findings of this study are available from the corresponding author, [Z. Yan], upon reasonable request.

References

[1] Elahinia M, Shayesteh Moghaddam N, Taheri Andani M, et al. Fabrication of NiTi through additive manufacturing: a review. Prog Mater Sci. 2016;83:630–663. doi:10.1016/j.pmatsci.2016.08.001
[2] Wang X, Yu J, Liu J, et al. Effect of process parameters on the phase transformation behavior and tensile properties of NiTi shape memory alloys fabricated by selective laser melting. Addit Manuf. 2020;36:101545. doi:10.1016/j.addma.2020.101545
[3] Gorgin Karaji Z, Speirs M, Dadbakhsh S, et al. Additively manufactured and surface biofunctionalized porous nitinol. ACS Appl Mater Interfaces. 2017;9:1293–1304. doi:10.1021/acsami.6b14026
[4] Lu HZ, Liu LH, Yang C, et al. Simultaneous enhancement of mechanical and shape memory properties by heat-treatment homogenization of Ti2Ni precipitates in TiNi shape memory alloy fabricated by selective laser melting. J Mater Sci Technol. 2022;101:205–216. doi:10.1016/j.jmst.2021.06.019
[5] Li X, Zhang B, Jakobi T, et al. Laser-based bionic manufacturing. Int J Extrem Manuf. 2024;6:042003. doi:10.1088/2631-7990/ad3f59

[6] Yan Z, Zhu J, Borisov E, et al. Superelastic response and damping behavior of additively manufactured nitinol architectured materials. Addit Manuf. 2023;68:103505. doi:10.1016/j.addma.2023.103505
[7] Xiong Z, Li M, Hao S, et al. 3D-Printing Damage-Tolerant architected metallic materials with shape recoverability via special deformation design of constituent material. ACS Appl Mater Interfaces. 2021;13:39915–39924. doi:10.1021/acsami.1c11226
[8] Yuan L, Gu D, Lin K, et al. Mechanical property enhancement in additively manufactured NiTi double-asymmetric honeycombs with bioinspired graded design. Virtual Phys Prototyp. 2024;19:e2321160. doi:10.1080/17452759.2024.2321160
[9] Weber R, Kuhlow M, Spierings AB, et al. 4D printed assembly of sensors and actuators in complex formed metallic lightweight structures. J Manuf Process. 2023;90:406–417. doi:10.1016/j.jmapro.2023.01.012
[10] Hartl DJ, Mooney JT, Lagoudas DC, et al. Use of a Ni60Ti shape memory alloy for active jet engine chevron application: II. Experimentally validated numerical analysis. Smart Mater Struct. 2010;19:015021. doi:10.1088/0964-1726/19/1/015021
[11] Tan C, Zou J, Li S, et al. Additive manufacturing of bio-inspired multi-scale hierarchically strengthened lattice structures. Int J Mach Tools Manuf. 2021;167:103764. doi:10.1016/j.ijmachtools.2021.103764
[12] Yang X, Yang Q, Shi Y, et al. Effect of volume fraction and unit cell size on manufacturability and compressive behaviors of Ni-Ti triply periodic minimal surface lattices. Addit Manuf. 2022;54:102737. doi:10.1016/j.addma.2022.102737
[13] Lu HZ, Ma HW, Luo X, et al. Microstructure, shape memory properties, and in vitro biocompatibility of porous NiTi scaffolds fabricated via selective laser melting. J Mater Res Technol. 2021;15:6797–6812. doi:10.1016/j.jmrt.2021.11.112
[14] Großmann A, Felger J, Frölich T, et al. Melt pool controlled laser powder bed fusion for customised low-density lattice structures. Mater Des. 2019;181:108054. doi:10.1016/j.matdes.2019.108054
[15] Delroisse P, Jacques PJ, Maire E, et al. Effect of strut orientation on the microstructure heterogeneities in AlSi10Mg lattices processed by selective laser melting. Scr Mater. 2017;141:32–35. doi:10.1016/j.scriptamat.2017.07.020
[16] Gibson LJ, Ashby MF. Mechanics of three-dimensional cellular materials. Proc R Soc London, Ser A Math Phys Sci. 1982;382:43–59. doi:10.1098/rspa.1982.0088
[17] Saedi S, Shayesteh Moghaddam N, Amerinatanzi A, et al. On the effects of selective laser melting process parameters on microstructure and thermomechanical response of Ni-rich NiTi. Acta Mater. 2018;144:552–560. doi:10.1016/j.actamat.2017.10.072
[18] Xue L, Atli KC, Picak S, et al. Controlling martensitic transformation characteristics in defect-free NiTi shape memory alloys fabricated using laser powder bed fusion and a process optimization framework. Acta Mater. 2021;215:117017. doi:10.1016/j.actamat.2021.117017
[19] Safdel A, Zaker N, Botton GA, et al. The role of texture and restoration mechanisms in defining the tension-compression asymmetry behavior of aged NiTi alloys fabricated by laser powder bed fusion. Mater Sci Eng A. 2023;864:144592. doi:10.1016/j.msea.2023.144592
[20] Lu HZ, Liu LH, Luo X, et al. Formation mechanism of heterogeneous microstructures and shape memory effect in NiTi shape memory alloy fabricated via laser powder bed fusion. Mater Des. 2023;232:112107. doi:10.1016/j.matdes.2023.112107
[21] Xue L, Atli KC, Zhang C, et al. Laser powder Bed fusion of defect-free NiTi shape memory alloy parts with superior tensile superelasticity. Acta Mater. 2022;229:117781. doi:10.1016/j.actamat.2022.117781
[22] Zhu JN, Liu K, Riemslag T, et al. Achieving superelasticity in additively manufactured Ni-lean NiTi by crystallographic design. Mater Des. 2023;230:111949. doi:10.1016/j.matdes.2023.111949
[23] Tan C, Li S, Essa K, et al. Laser powder Bed fusion of Ti-rich TiNi lattice structures: process optimisation, geometrical integrity, and phase transformations. Int J Mach Tools Manuf. 2019;141:19–29. doi:10.1016/j.ijmachtools.2019.04.002
[24] Jamshidi P, Panwisawas C, Langi E, et al. Development, characterisation, and modelling of processability of nitinol stents using laser powder bed fusion. J Alloys Compd. 2022;909:164681. doi:10.1016/j.jallcom.2022.164681
[25] Safdel A, Torbati-Sarraf H, Elbestawi MA. Laser powder bed fusion of differently designed NiTi stent structures having enhanced recoverability and superelasticity. J Alloys Compd. 2023;954:170196. doi:10.1016/j.jallcom.2023.170196
[26] Niendorf T, Brenne F, Schaper M. Lattice structures manufactured by SLM: on the effect of geometrical dimensions on microstructure evolution during processing. Metall Mater Trans B Process Metall Mater Process Sci. 2014;45:1181–1185. doi:10.1007/s11663-014-0086-z
[27] Britt C, Montgomery CJ, Brand MJ, et al. Effect of processing parameters and strut dimensions on the microstructures and hardness of stainless steel 316L lattice-emulating structures made by powder bed fusion. Addit Manuf. 2021;40:101943. doi:10.1016/j.addma.2021.101943
[28] Liu M, Takata N, Suzuki A, et al. Development of gradient microstructure in the lattice structure of AlSi10Mg alloy fabricated by selective laser melting. J Mater Sci Technol. 2020;36:106–117. doi:10.1016/j.jmst.2019.06.015
[29] Banait S, Liu C, Campos M, et al. Coupled effect of microstructure and topology on the mechanical behavior of Inconel718 additively manufactured lattices. Mater Des. 2022;224:111294. doi:10.1016/j.matdes.2022.111294
[30] Wauthle R, Vrancken B, Beynaerts B, et al. Effects of build orientation and heat treatment on the microstructure and mechanical properties of selective laser melted Ti6Al4 V lattice structures. Addit Manuf. 2015;5:77–84. doi:10.1016/j.addma.2014.12.008
[31] Zhang J, Liu Y, Babamiri BB, et al. Enhancing specific energy absorption of additively manufactured titanium lattice structures through simultaneous manipulation of architecture and constituent material. Addit Manuf. 2022;55:102887. doi:10.1016/j.addma.2022.102887
[32] Johnson NS, Strantza M, Matthews MJ, et al. Direct measurement of the effective properties of an additively manufactured titanium octet truss unit cell using high energy X-ray diffraction, Mater Charact. 2024;209:113755. doi:10.1016/j.matchar.2024.113755

[33] Oliveira JP, Strantza RM, Braz Fernandes MF, Welding and joining of NiTi shape memory alloys: a review, Prog Mater Sci. 88 (2017) 412–466. doi:10.1016/j.pmatsci.2017.04.008
[34] Safaei K, Nematollahi M, Bayati P, et al. On the crystallographic texture and torsional behavior of NiTi shape memory alloy processed by laser powder bed fusion: effect of build orientation, Addit Manuf. 2022;59:103184. doi:10.1016/j.addma.2022.103184
[35] Li B, Wang L, Wang B, et al. Solidification characterization and its correlation with the mechanical properties and functional response of NiTi shape memory alloy manufactured by electron beam freeform fabrication. Addit Manuf. 2021;48:102468. doi:10.1016/j.addma.2021.102468
[36] Mehrpouya M, Gisario A, Brotzu A, et al. Laser welding of NiTi shape memory sheets using a diode laser. Opt Laser Technol. 2018;108:142–149. doi:10.1016/j.optlastec.2018.06.038
[37] Lu HZ, Ma HW, Cai WS, et al. Stable tensile recovery strain induced by a Ni4Ti3 nanoprecipitate in a Ni50.4Ti49.6 shape memory alloy fabricated via selective laser melting. Acta Mater. 2021;219:117261. doi:10.1016/j.actamat.2021.117261
[38] Cisse C, Zaki W, Zineb TB. A review of constitutive models and modeling techniques for shape memory alloys. Int J Plast. 2016;76:244–284. doi:10.1016/j.ijplas.2015.08.006
[39] Auricchio F, Taylor RL, Lubliner J. Shape-memory alloys: macromodelling and numerical simulations of the superelastic behavior. Comput Methods Appl.Mech Eng. 1997;146:281–312. doi:10.1016/S0045-7825(96)01232-7
[40] Lagoudas D, Hartl D, Chemisky Y, et al. Constitutive model for the numerical analysis of phase transformation in polycrystalline shape memory alloys. Int J Plast. 2012;32–33:155–183. doi:10.1016/j.ijplas.2011.10.009
[41] Lagoudas DC. *Shape memory alloys: modeling and engineering applications*. New York: Springer; 2008.
[42] Hartl DJ, Lagoudas DC, Calkins FT, et al. Use of a Ni60Ti shape memory alloy for active jet engine chevron application: I. Thermomechanical characterization. Smart Mater Struct. 2010;19:015020. doi:10.1088/0964-1726/19/1/015020
[43] An N, Li M, Zhou J. Modeling SMA-enabled soft deployable structures for kirigami/origami reflectors. Int J Mech Sci. 2020;180:105753. doi:10.1016/j.ijmecsci.2020.105753
[44] Tancogne-Dejean T, Spierings AB, Mohr D. Additively-manufactured metallic micro-lattice materials for high specific energy absorption under static and dynamic loading. Acta Mater. 2016;116:14–28. doi:10.1016/j.actamat.2016.05.054
[45] Machado G, Louche H, Alonso T, et al. Superelastic cellular NiTi tube-based materials: fabrication, experiments and modeling. Mater Des. 2015;65:212–220. doi:10.1016/j.matdes.2014.09.007
[46] Saedi S, Saghaian SE, Jahadakbar A, et al. Shape memory response of porous NiTi shape memory alloys fabricated by selective laser melting. J Mater Sci Mater Med. 2018;29:40. doi:10.1007/s10856-018-6044-6
[47] Li X, Li Q, Nie M, et al. Evading the strength-ductility trade-off dilemma in steel-nickel heterostructured material by bionic crossed-lamellar structures. Virtual Phys Prototyp. 2023;18:e2266640. doi:10.1080/17452759.2023.2266640
[48] Jiang H, Wang X, Xi R, et al. Size effect on the microstructure, phase transformation behavior, and mechanical properties of NiTi shape memory alloys fabricated by laser powder bed fusion. J Mater Sci Technol. 2023;157:200–212. doi:10.1016/j.jmst.2023.02.026
[49] Dadbakhsh S, Speirs M, Kruth JP, et al. Influence of SLM on shape memory and compression behaviour of NiTi scaffolds. CIRP Ann - Manuf Technol. 2015;64:209–212. doi:10.1016/j.cirp.2015.04.039
[50] Martin AA, Calta NP, Khairallah SA, et al. Dynamics of pore formation during laser powder bed fusion additive manufacturing. Nat Commun. 2019;10:1–10. doi:10.1038/s41467-019-10009-2
[51] DebRoy T, Wei HL, Zuback JS, et al. Additive manufacturing of metallic components – process, structure and properties. Prog Mater Sci. 2018;92:112–224. doi:10.1016/j.pmatsci.2017.10.001
[52] Thompson SM, Bian L, Shamsaei N, et al. An overview of direct laser deposition for additive manufacturing; part I: transport phenomena, modeling and diagnostics. Addit Manuf. 2015;8:36–62. doi:10.1016/j.addma.2015.07.001
[53] Mukherjee T, Manvatkar V, De A, et al. Dimensionless numbers in additive manufacturing. J Appl Phys. 2017;121:064904. doi:10.1063/1.4976006
[54] McMillan M, Leary M, Brandt M. Computationally efficient finite difference method for metal additive manufacturing: a reduced-order DFAM tool applied to SLM. Mater Des. 2017;132:226–243. doi:10.1016/j.matdes.2017.06.058
[55] Tancogne-Dejean T, Mohr D. Stiffness and specific energy absorption of additively-manufactured metallic BCC metamaterials composed of tapered beams. Int J Mech Sci. 2018;141:101–116. doi:10.1016/j.ijmecsci.2018.03.027
[56] Cheng B, Price S, Lydon J, et al. On process temperature in powder-Bed electron beam additive manufacturing: model development and validation. J Manuf Sci Eng Trans ASME. 2014;136:1–12. doi:10.1115/1.4028484
[57] Hocine S, Van Swygenhoven H, Van Petegem S. Verification of selective laser melting heat source models with operando X-ray diffraction data. Addit Manuf. 2021;37:101747. doi:10.1016/j.addma.2020.101747
[58] Wolfer AJ, Aires J, Wheeler K, et al. Fast solution strategy for transient heat conduction for arbitrary scan paths in additive manufacturing. Addit Manuf. 2019;30:100898. doi:10.1016/j.addma.2019.100898
[59] Yang Y, van Keulen F, Ayas C. A computationally efficient thermal model for selective laser melting. Addit Manuf. 2020;31:100955. doi:10.1016/j.addma.2019.100955
[60] Wei LC, Ehrlich LE, Powell-Palm MJ, et al. Thermal conductivity of metal powders for powder bed additive manufacturing. Addit Manuf. 2018;21:201–208. doi:10.1016/j.addma.2018.02.002
[61] An N, Yang G, Yang K, et al. Implementation of abaqus user subroutines and plugin for thermal analysis of powder-bed electron-beam-melting additive manufacturing process. Mater Today Commun. 2021;27:102307. doi:10.1016/j.mtcomm.2021.102307
[62] Yan Z, Liu W, Tang Z, et al. Review on thermal analysis in laser-based additive manufacturing. Opt Laser

Technol. 2018;106:427–441. doi:10.1016/j.optlastec.2018.04.034

[63] Hagenlocher C, O'Toole P, Xu W, et al. Analytical modelling of heat accumulation in laser based additive manufacturing processes of metals. Addit Manuf. 2022;60:103263. doi:10.1016/j.addma.2022.103263

[64] Zhu JN, Borisov E, Liang X, et al. Predictive analytical modelling and experimental validation of processing maps in additive manufacturing of nitinol alloys. Addit Manuf. 2021;38:101802. doi:10.1016/j.addma.2020.101802

[65] Khalil Allafi J, Ren X, Eggeler G. The mechanism of multistage martensitic transformations in aged Ni-rich NiTi shape memory alloys. Acta Mater. 2002;50:793–803. doi:10.1016/S1359-6454(01)00385-8

[66] Mehrpouya M, Gisario A, Elahinia M. Laser welding of NiTi shape memory alloy: a review. J Manuf Process. 2018;31:162–186. doi:10.1016/j.jmapro.2017.11.011

[67] Gäumann M, Bezençon C, Canalis P, et al. Single-crystal laser deposition of superalloys: processing-microstructure maps. Acta Mater. 2001;49:1051–1062. doi:10.1016/S1359-6454(00)00367-0

[68] Hooper PA. Melt pool temperature and cooling rates in laser powder bed fusion. Addit Manuf. 2018;22:548–559. doi:10.1016/j.addma.2018.05.032

[69] Leung CLA, Marussi S, Atwood RC, et al. In situ X-ray imaging of defect and molten pool dynamics in laser additive manufacturing. Nat Commun. 2018;9:1–9. doi:10.1038/s41467-017-02088-w